AIAA JOURNAL
Vol. 42, No. 10, October 2004

Unsteady Three-Dimensional Viscous Flow Simulation of a Dragonfly Hovering

Koji Isogai,* Shun Fujishiro,† Taku Saitoh,† Manabu Yamamoto,† Masahide Yamasaki,‡ and Manabu Matsubara‡
Kyushu University, Fukuoka 812-8581, Japan

To clarify the basic aerodynamic mechanisms of the hovering flight of the dragonfly, numerical simulations of the unsteady viscous flow around a tandem wing configuration have been performed using a three-dimensional Navier–Stokes code. The flow simulations are conducted for *Anax parthenope julius* as a typical dragonfly model. The total lifting force and specific necessary power predicted by the present simulation show close agreement with those observed experimentally for the present dragonfly model. The present code is further validated by comparing the results of the simulation with the experimental values of total lift and stroke-plane angle obtained using a robot.

I. Introduction

THE dragonfly can hover while maintaining its body axis almost horizontal.[1] The aerodynamic mechanism behind this ability is not yet fully understood, although several experimental and theoretical studies[2–15] have been conducted thus far. However, previous theoretical studies have been confined to the two-dimensional quasi-steady/unsteady aerodynamics of single airfoil[6–9,11]/tandem airfoil configurations.[10,12–15] Among these, the numerical studies on the tandem airfoil configuration using a two-dimensional Navier–Stokes (NS) code revealed much about the mechanism, in particular, the flow interaction problem between the fore- and hindwings. Isogai and Shinmoto[10,12] analyzed the unsteady viscous flow around a tandem airfoil configuration at a typical spanwise station of dragonfly wings by assuming the flow to be locally two dimensional, and they showed that mutual interaction is fundamental in generating the time-mean aerodynamic force acting in the direction of the stroke plane, which is indispensable in order for the dragonfly to be able to hover with the body axis horizontal. Kim and Choi[14] have also investigated the mutual interaction problem by employing an immersed boundary method in Cartesian coordinates. In their analyses, special consideration was given to the effect of the phase difference of the flapping motions of the fore- and hindwings, and the maximum lifting force was shown to be generated at zero phase difference.

Although these studies using two-dimensional NS codes did shed some light on the mechanism, the important, three-dimensional effects have been neglected thus far. As a result, the total aerodynamic forces and the necessary power for hovering flight, which are estimated using two-dimensional strip aerodynamics, become uncertain. Simulations using the three-dimensional NS code are necessary in order to investigate the aerodynamic mechanism of hovering flight of the dragonfly in greater detail. A numerical study of the hovering of the hawkmoth using the three-dimensional NS code was presented by Liu et al.,[16] but three-dimensional NS simulations of dragonfly hovering have not yet been reported. The present paper introduces the first three-dimensional NS simulation of dragonfly hovering. The method employed herein is an extension of the method employed by Isogai and Shinmoto in their two-dimensional NS simulation of a tandem airfoil configuration.[12] In the following sections, the numerical method, the results of computation, and the code validation are presented.

Received 4 November 2003; revision received 22 March 2004; accepted for publication 29 April 2004; presented as Paper 2004-2717 at the AIAA 34th Fluid Dynamics Conference, Portland, OR, 28 June–1 July 2004.

*Professor, Department of Aeronautics and Astronautics, 6-10-1 Hakozaki, Higashiku; isogai@acro.kyushu-u.ac.jp. Associate Fellow AIAA.
†Graduate Student, Department of Aeronautics and Astronautics, 6-10-1 Hakozaki, Higashiku.
‡Research Assistant, Department of Aeronautics and Astronautics, 6-10-1 Hakozaki, Higashiku.

II. Method of Analysis

The definitions of the coordinates and forces are shown in Fig. 1. The Y axis is taken in the direction of the stroke plane, and the X axis is taken in the direction perpendicular to the Y axis. The fore- and hindwings are assumed to be oscillating in a coupled flapping and feathering mode, in which the feathering oscillation advances 90 deg ahead of the flapping osillation.[3] There is also some phase difference between the flapping motions of fore- and hindwings. In the present study, this phase difference is changed as a parameter. For the aerodynamic forces acting on the dragonfly in the hovering flight condition, we define $\overline{L_Y}$ and $\overline{L_X}$ (Fig. 1), where $\overline{L_Y}$ is the mean aerodynamic force (time mean value of L_Y during one cycle of oscillation) acting in the direction of the Y axis and $\overline{L_X}$ is the time mean aerodynamic forces acting in the negative direction of the X axis. Then, the lifting force $\overline{L_{\text{hover}}}$, which is equal to the body weight, is given by $\overline{L_{\text{hover}}} = \sqrt{(\overline{L_X}^2 + \overline{L_Y}^2)}$. The stroke-plane angle ϕ_s (Fig. 1) can be given by $\phi_s = \tan^{-1}(\overline{L_Y}/\overline{L_X})$.

The physical space around a tandem wing configuration is shown in Fig. 2. The y axis is taken in the direction of the stroke plane as already described. The z axis is taken in the spanwise direction. The wings are assumed to be flat plates of zero thickness. The three-dimensional compressible Navier–Stokes equations are applied for the numerical simulations of the unsteady viscous flow around the oscillating tandem wing configuration, as shown in Fig. 2a. All of the physical quantities in the NS equations are nondimensionalized by the semichord length b_f, the maximum heaving velocity V_f (which is caused by the flapping oscillation) at the 75% semispan station of the forewing, and the air density. The similarity parameters that govern the unsteady viscous flow around the present tandem wing configuration in hover mode are Reynolds number and the reduced frequency.

Reynolds number R and the reduced frequency k are defined as

$$R = (b_f V_f)/\nu \tag{1}$$

$$k = (b_f \omega)/V_f \tag{2}$$

where ν is the kinematic viscosity and ω is the circular frequency of oscillation. Because V_f can be given by $V_f = \omega H_{f0}$, where H_{f0} is the heaving amplitude of the forewing (at the location of the feathering axis) at the 75% semispan station, k can also be expressed as

$$k = b_f/H_{f0} \tag{3}$$

The motions of the fore- and hindwings, which are coupled flapping and feathering motions, can be expressed as the displacements of the wing surfaces in the y direction as follows.

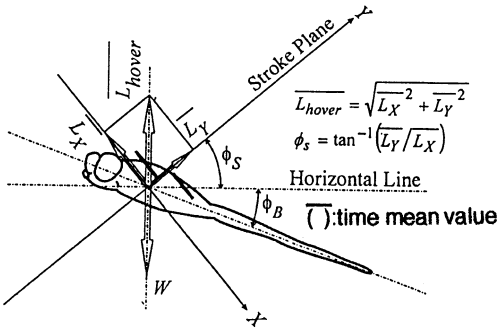

Fig. 1 Definitions of coordinates and forces.

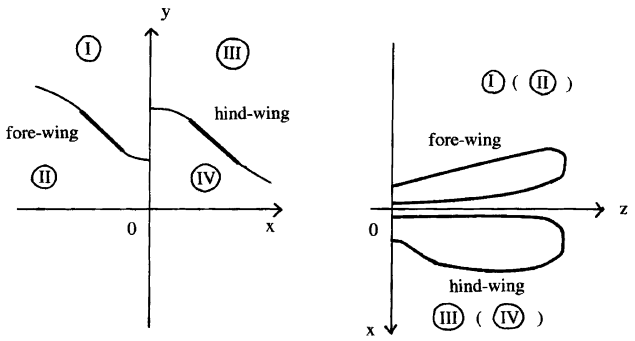

Fig. 2a Physical spaces.

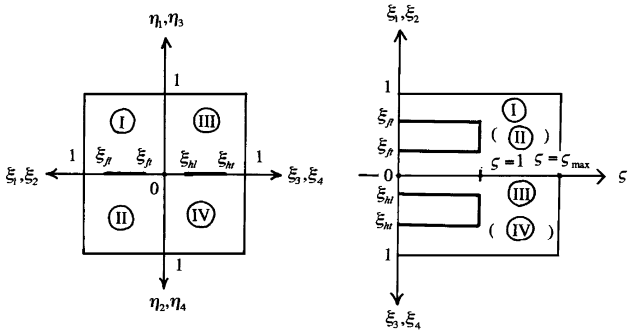

Fig. 2b Computational spaces.

Forewing:

$$y = (h_{r,f} + \phi_{0,f} z)\sin kt - (\theta_{r,f} + b_{\theta,f} z)[x - x_{p,f}(z)]\sin(kt + \phi_f) \quad (4)$$

Hindwing:

$$y = (h_{r,h} + \phi_{0,h} z)\sin(kt + \Psi) - (\theta_{r,h} + b_{\theta,h} z)[x - x_{p,h}(z)]\sin(kt + \phi_f + \Psi) \quad (5)$$

where t is the dimensionless time, h_r is the heaving displacement at the root station, ϕ_0 is the amplitude of flapping oscillation, θ_r is the amplitude of pitching oscillation at the root station, the amplitude of the pitching oscillation is assumed to increase linearly toward the tip station with the slope of b_θ, x_p is the x coordinate of the pitch axis, and ϕ is the phase advance angle of the feathering oscillation ahead of the flapping oscillation. In Eqs. (4) and (5), the suffixes f and h indicate forewing and hindwing, respectively.

To cope with the present two-wing problem, in which each wing moves differently, a multiblock method is employed. The physical space is divided into four sectors, denoted as I, II, III, and IV, as shown in Fig. 2a. Each sector in the physical space, which moves and deforms with time in accordance with the wing motion, is mapped on each corresponding sector in the computational space, as shown in Fig. 2b. Each of these four blocks in the computational space is a rectangular parallelepiped, and the planform of each wing becomes rectangular. A rectangular grid system with constant grid spacing is adapted to each computational domain. Each computational domain is mapped on the corresponding physical domain at each time step using algebraic mapping functions. The regridding is performed so that the local chord length of the fore- and hindwings is unchanged while each wing flaps and rotates about its feathering axis.

The time-differenced form of the geometric conservation law[17] coupled with the conservation form of the three-dimensional NS equations in each computational space is solved at each time step. The implicit time-integration algorithm without inner iteration is used, and Courant number near the body is taken to be 0.75 so that the time accuracy of the computation is maintained. The total-variation-diminishing scheme[18] is employed to solve the NS equations. The far-field boundaries are located at 15 chord lengths away from the wing in the X and Y directions and five semispan lengths away in the Z direction. (In Ref. 16, in which the hawkmoth hovering is computed, the far-field boundary is located at six mean chord lengths away from the wing.) At these boundaries, the flow quantities are given by the zero-order extrapolation from the inner points. At the $z = 0$ plane, the symmetry conditions are applied. At the boundaries where the united domain of I and II and that of III and IV overlap, the flow quantities at the grid points of each domain should be interpolated in order to exchange information because these areas overlap each other based on the wing motions in the physical space, and we employed the linear interpolation scheme. At the wing surfaces, the no-slip conditions[19] are given. A total of $260 \times 60 \times 35$ grid points is used for the whole flowfield. The number of grid points on the upper/lower-wing surfaces of the fore/hindwings are 60 points in chordwise and 25 points in spanwise directions, respectively. The number of grid points in the direction normal to the upper/lower surfaces are 30 in each direction, respectively. As seen in the next section, the number of grid points seems to be enough for the resolution of the flowfield, especially the vortices induced by the flapping motions of the wings in still air. For all flow computations, the Mach number is assumed to be 0.10, and a no-turbulence model is used because the Reynolds number is on the order of 10^3.

III. Dragonfly Model and Results of Simulation

In the present simulation, we used *Anax parthenope julius* as a typical dragonfly. According to the observations of Azuma and Watanabe,[3] the full-span length of forewing is approximately 0.10 m, and the aspect ratio is 10. The planforms of the fore- and hindwings used in the present computations are shown in Fig. 3. The flapping axis and the feathering axes of the fore- and hindwings are also shown in the figure. The semichord length at the 75% semispan station of the forewing is 0.005 m, which is taken as the reference length b_f, as mentioned in Sec. II. (For computational purposes, the planforms near the root stations are somewhat modified compared to the actual dragonfly.) The flapping amplitudes of the fore- and hindwings, namely, $\phi_{0,f}$ and $\phi_{0,h}$, are taken to be 40 deg (Ref. 3).

The spanwise distributions of the feathering amplitude used in the present computations are shown in Fig. 4, where they are compared with the experimental data obtained by Azuma and Watanabe.[3] The feathering amplitudes differ depending on whether the wings are in upward or downward motion. The frequency of oscillation is

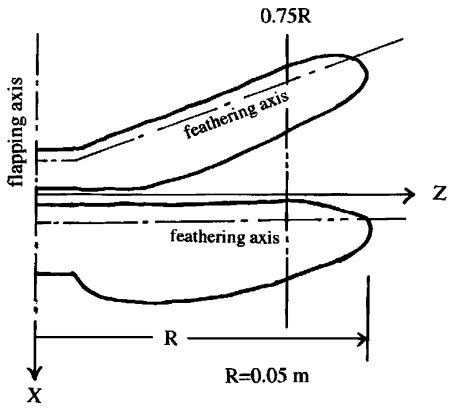

Fig. 3 Planform of dragonfly model.

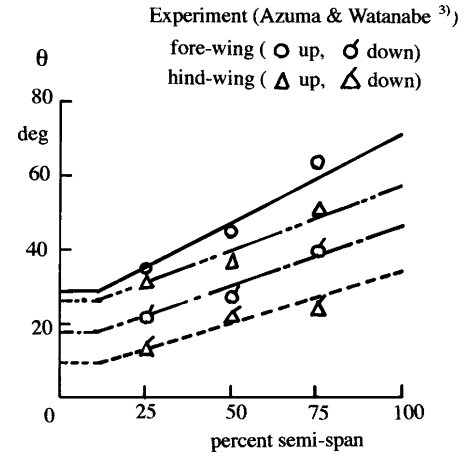

Fig. 4 Spanwise distributions of feathering amplitudes of fore- and hindwings.

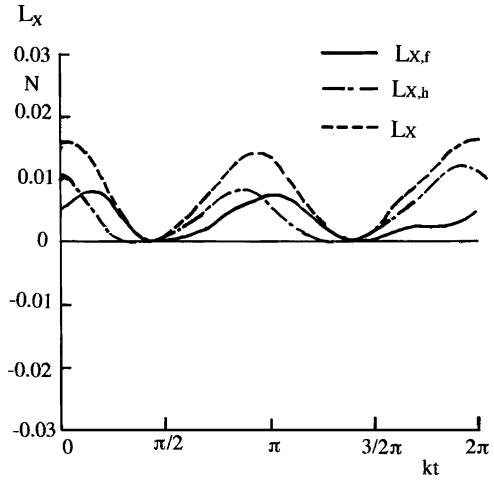

Fig. 6 Variation of L_X during one cycle of oscillation.

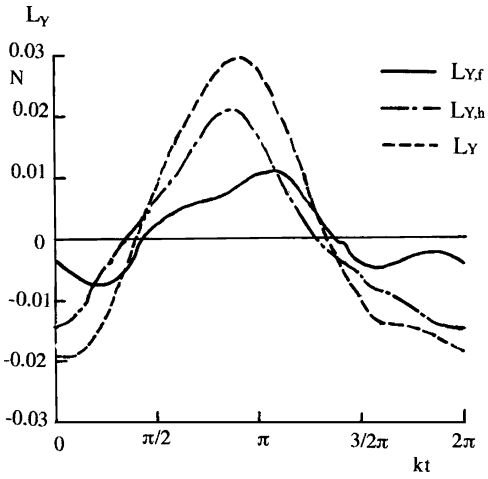

Fig. 5 Variation of L_Y during one cycle of oscillation.

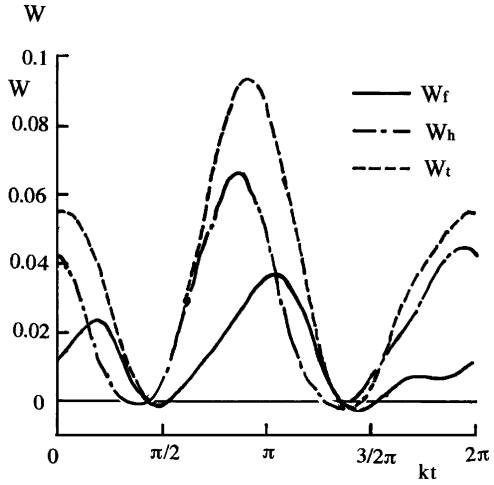

Fig. 7 Variation of W during one cycle of oscillation.

28 Hz (Ref. 3). The reference velocity V_f is then 4.24 m/s. The Reynolds number R and the reduced frequency k defined by Eqs. (1) and (2) are 1.45×10^3 and 0.207, respectively. The phase advance angles ϕ_f and ϕ_h of the feathering oscillations ahead of the flapping oscillations are both 90 deg (Ref. 3). The phase advance angle Ψ of the flapping oscillation of the hindwing ahead of the forewing is changed parametrically from $\Psi = 0$ to 80 deg.

The converged periodic solutions are usually obtained after three to four oscillation cycles. The convergence to a periodic solution is confirmed by the fact that the difference between the values for $\overline{L_{\text{hover}}}$ and ϕ_s obtained for the final two cycles of oscillation are less than 1% for $\overline{L_{\text{hover}}}$ and less than 1 deg for ϕ_s. Direct verification of the present NS simulation code has been performed by comparing the computed results with experimental data obtained using a robot.[15] These results will be presented in Sec. IV.

As a typical case for *Anax parthenope julius*, the results obtained for $\Psi = 20$ deg are presented in detail. The variations of the aerodynamic forces acting (in the direction of the stroke-plane) on the full span of the fore- and hindwings are shown in Fig. 5. $L_{Y,f}$ is that for the forewing, $L_{Y,h}$ is that for the hindwing, and L_Y is the sum of $L_{Y,f}$ and $L_{Y,h}$. The downward motion of the forewing is for the period of $kt = \pi/2 - 3/2\pi$, whereas the upward motion of the forewing is for the period of $kt = 0 - \pi/2$ and $kt = 3/2\pi - 2\pi$. The time mean values of $L_{Y,f}$, $L_{Y,h}$, and L_Y are as follows:

$$\overline{L_{Y,f}} = 0.835 \times 10^{-3} \text{ N}$$

$$\overline{L_{Y,h}} = 1.176 \times 10^{-3} \text{ N}$$

$$\overline{L_Y} = 2.012 \times 10^{-3} \text{ N}$$

The variations of the aerodynamic forces ($L_{X,f}$, $L_{X,h}$, L_X) acting (in the negative x direction, perpendicular to the stroke-plane) on the full span of the fore- and hindwings are shown in Fig. 6. The time mean values of $L_{X,f}$, $L_{X,h}$, and L_X are as follows:

$$\overline{L_{X,f}} = 3.343 \times 10^{-3} \text{ N}$$

$$\overline{L_{X,h}} = 4.456 \times 10^{-3} \text{ N}$$

$$\overline{L_X} = 7.908 \times 10^{-3} \text{ N}$$

The variations of the rates of work (W_f, W_h, W_t) consumed by the full span of the fore- and hindwings during one cycle of oscillation are shown in Fig. 7. The time mean values of W_f, W_h, and W_t are as follows:

$$\overline{W_f} = 1.299 \times 10^{-2} \text{ W}$$

$$\overline{W_h} = 2.463 \times 10^{-2} \text{ W}$$

$$\overline{W_t} = 3.764 \times 10^{-2} \text{ W}$$

The vector sum of $\overline{L_Y}$ and $\overline{L_X}$ gives $\overline{L_{\text{hover}}}$, which balances with the weight of the dragonfly and becomes

$$\overline{L_{\text{hover}}} = 8.160 \times 10^{-3} \text{ N}$$

The stroke-plane angle of ϕ_s can be obtained by $\phi_s = \tan^{-1}(\overline{L_Y}/\overline{L_X})$, which then becomes

$$\phi_s = 14.3 \text{ deg}$$

Because the weight of *Anax parthenope julius*[3] is 7.74×10^{-3} N, the predicted value of $\overline{L_{\text{hover}}}$ is slightly greater than the weight of the dragonfly, and so the lift force can sustain the weight of the dragonfly. The load factor n becomes 1.054. We can easily estimate the necessary power for 1-g hover using the relation[12] $P_n' = W_t/n^{1.5}$ as $P_n' = 3.477 \times 10^{-2}$ W. The available power P_a of an insect is usually estimated using the following formulas[20]:

$$P_a/m_m = 260 \text{ W/kg}, \qquad m_m/m = \tfrac{1}{4}$$

where m_m is the muscular mass of the insect and m is the total mass of the insect. When we apply these relations to *Anax parthenope julius*, the available power is estimated to be $P_a = 5.14 \times 10^{-2}$ W, which is higher than the necessary power of 3.477×10^{-2} W estimated by the present NS simulation. It is also easy to estimate the specific necessary power (necessary power for 1 kg of muscular mass), which is 191 W/kg. (We can also estimate the necessary power for 1 kg of mass as 47.7 W/kg.) These values are quite reasonable when compared with those estimated by other researchers.[9]

The spanwise distributions of the time mean values of the section forces acting in the direction of the stroke plane, namely, $\overline{l_{Y,f}}$ and $\overline{l_{Y,h}}$, are plotted in Fig. 8. Similarly, the time mean section forces acting in the negative direction of the X axis, namely, $\overline{l_{X,f}}$ and $\overline{l_{X,h}}$, are plotted in Fig. 9. To see the correlations between these aerodynamic forces and the instantaneous flow patterns qualitatively, the isovorticity $[\omega_z = (\partial v/\partial x - \partial u/\partial y)/2]$ contours in x–y plane at the three typical span stations, namely, 24, 49, and 76% semispan stations at $kt = \pi$ (downward motion) and at $kt = 2\pi$ (upward motion), are plotted in Figs. 10.

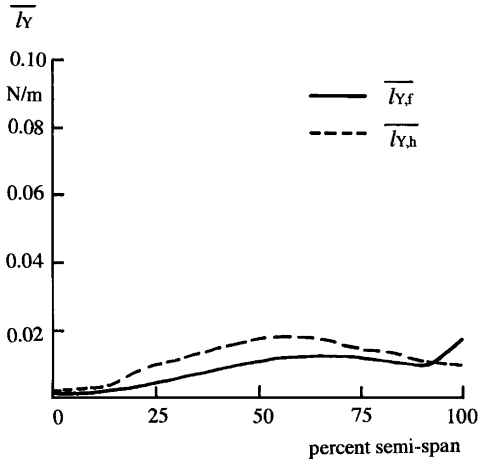

Fig. 8 Spanwise distributions of $\overline{l_Y}$.

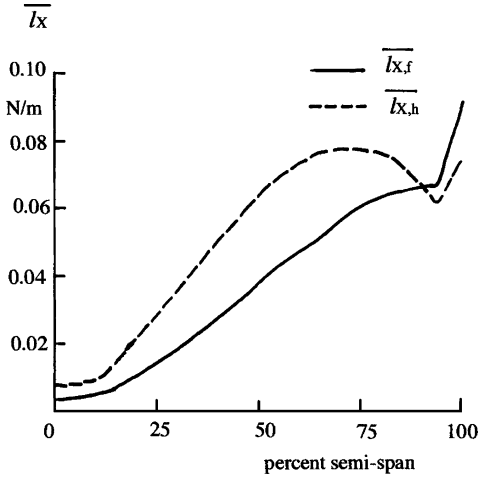

Fig. 9 Spanwise distributions of $\overline{l_X}$.

In both the downward and upward motions, strong leading-edge vortices are formed on the upper and lower surfaces, respectively, and the suction forces induced by these vortices seem to contribute to the generation of $\overline{l_{X,f}}$ and $\overline{l_{X,h}}$, whereas $\overline{l_{Y,f}}$ and $\overline{l_{Y,h}}$ appear to be generated by the asymmetric flow patterns between the downward and upward motions, which are caused by the differences in feathering amplitudes between the upward and downward motions, respectively. The sharp increase of $\overline{l_{X,f}}$ near the tip region, as seen in Fig. 9 is caused by the streamwise vorticity $[\omega_x = (\partial w/\partial y - \partial v/\partial z)/2]$ formed near the tip region. This is confirmed in Fig. 11, in which the isovorticity contour ω_x in the y–z plane along the midchord line of the forewing at $kt = \pi$ (in downward motion) is plotted.

To observe the effects of the phase angle Ψ between the flapping motions of the fore- and hindwings, numerical simulations have also been conducted for $\Psi = 0$, 40, 60, 80 deg in addition to $\Psi = 20$ deg. The variations of $\overline{L_{\text{hover}}}$, ϕ_s, and $\overline{W_t}$ with respect to Ψ are plotted in Fig. 12. In the figure, $\overline{L_{\text{hover}}}$ shows the maximum value of 8.66×10^{-3} N for $\Psi = 0$ deg, whereas ϕ_s shows the maximum value of 14.3 deg for $\Psi = 20$ deg. $\overline{L_{\text{hover}}}$ decreases gradually with the increase of Ψ, showing 7.00×10^{-3} N for $\Psi = 80$ deg. As already shown for $\Psi = 20$ deg, it is easy to estimate the necessary power P_n' for 1-g hover for these cases as well. The results are shown in Fig. 13, in which the available power of the present dragonfly model is also plotted by the solid line. The figure indicates that there is considerable available power for 1-g hovering of the present dragonfly model for all phase angles Ψ computed and that $\Psi = 0$ deg is the best for efficient hovering flight.

IV. Code Validation by Comparison with Experimental Data

To obtain the experimental data for evaluating the computational-fluid-dynamics code developed for simulating the unsteady viscous flow around the tandem wing configuration of the hovering dragonfly, we have developed a robot[15] that can hover in the water.

Although the development of a dragonfly robot that can hover in the air is extremely difficult, the development of a dragonfly robot that can hover in water is feasible because the buoyancy can sustain most of the weight of the robot. The basic idea is that the buoyancy and the lift generated by the flapping motions of the wings balance the body weight. The similarity parameters k and R are approximately matched between the robot and the present dragonfly model (*Anax parthenope julius*). As described later, the total weight of the robot is approximately 70 N, and the lifting force generated by the flapping motions of the wings is designed to be 5–10% of the total weight. The time mean lifting force can be accurately determined by directly measuring the weight of the robot submerged in the water just after it achieved perfect hovering. In Fig. 14, the photograph of the present robot is shown. The body is a cube of 0.252 m × 0.152 m × 0.172 m, and the total weight is approximately 70 N. The robot has two pairs of rectangular flat-plate wings, the planforms and sizes of which are shown in Fig. 15. The size of the wing is approximately three times larger than the present dragonfly model. As seen in Fig. 15, the flapping axis is located 0.019 m inside the body surface, and a gap of 0.035 m exists between the body surface and the root chords of the wings. The flapping amplitude of the forewing is 35.5 deg, and that of the hindwing is 30.5 deg. The feathering amplitudes of both wings are the same and are set at 64 and 40 deg for the upward and downward motions, respectively, and the angles are constant along the span. The axis of pitch is located at the 25% chord line for each wing. The four wings are actuated by eight servomotors. The two motors for each wing are used for flapping and feathering motions, respectively. The motions of the four wings are radio controlled by a laptop computer located outside of the water tank in which the hovering test is performed. The size of the water tank is a 1.0 m × 1.8 m × 0.5 m (height × width × depth), and the depth of the water is 0.45 m. The phase advance angle of the feathering motion ahead of the flapping motion of each wing is fixed at 90 deg, while the phase advance angle of the flapping motion of the hindwing ahead of the forewing can be set at an arbitrary value from 0 to 40 deg. The geometrical stroke-plane angle of each wing is set at 20 deg. The hovering test of the robot has

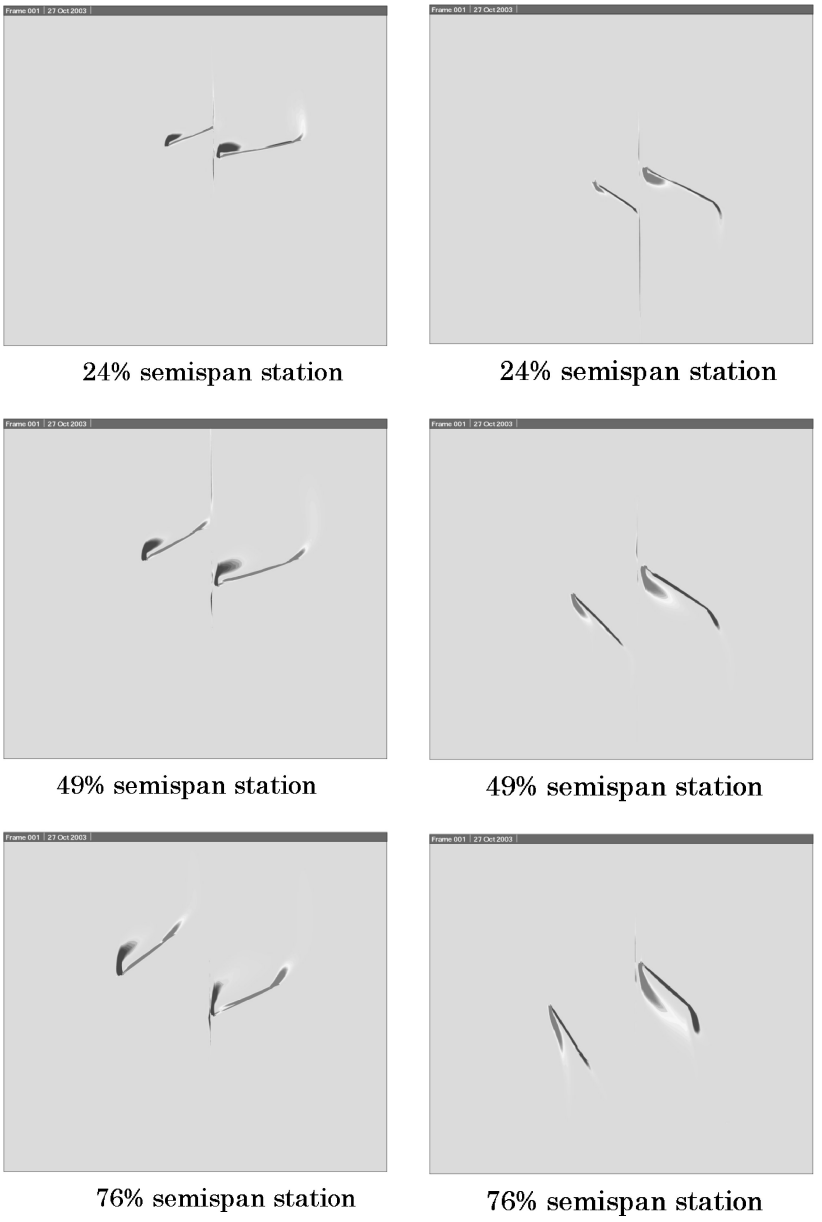

a) $kt = \pi$ (downward) b) $kt = 2\pi$ (upward)

Fig. 10 Isovorticity contours (ω_z) at three spanwise stations is downward and upward motions (ω_z: from −2 to 2).

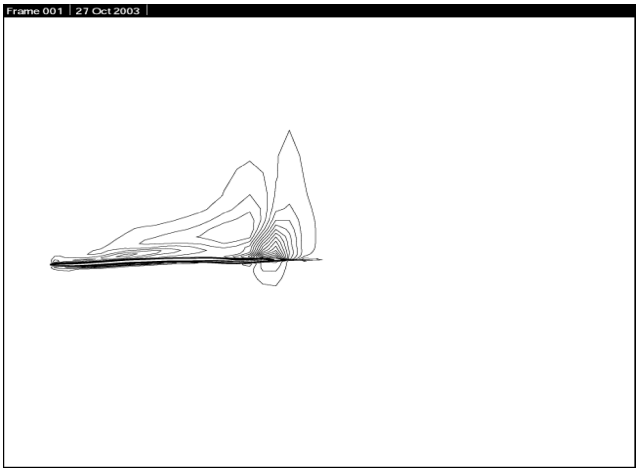

Fig. 11 Isovorticity contours (ω_x) along the midchord line of forewing (ω_x: from −1 to 1) at $kt = \pi$ (downward motion).

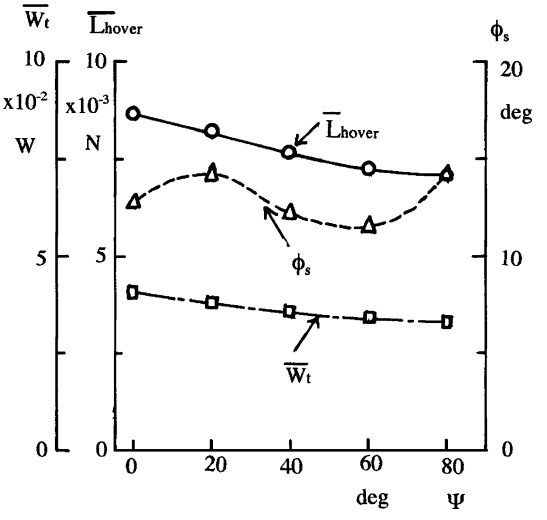

Fig. 12 Behaviors of $\overline{L_{hover}}$, ϕ_s, and $\overline{W_t}$ with respect to Ψ.

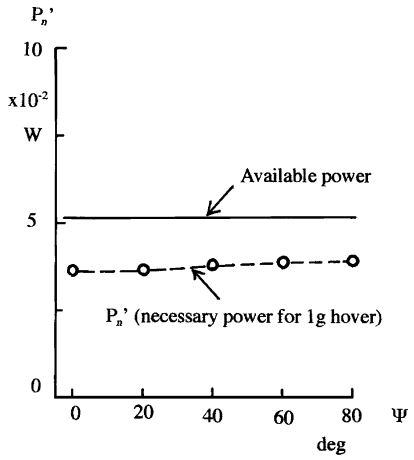

Fig. 13 Behavior of necessary power for 1-*g* hover with respect to Ψ.

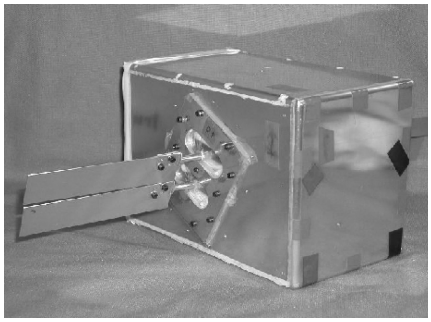

Fig. 14 Photograph of robot.

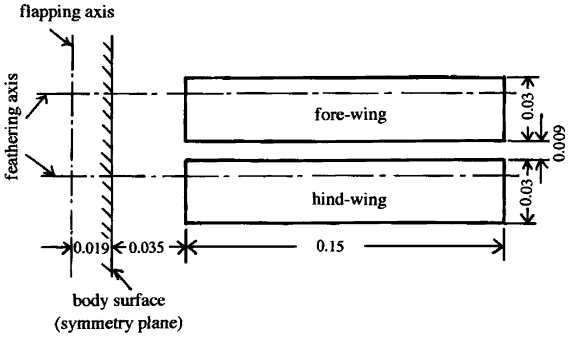

Fig. 15 Planforms of the fore- and hindwings of the robot.

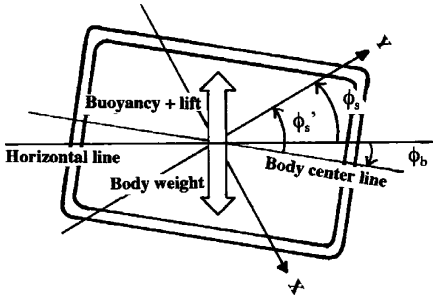

Fig. 16 Definition of stroke-plane angle in hovering condition.

been conducted at six different phase angles between the fore- and hindwings, that is, $\Psi = 0$, 10, 20, 30, 35, and 40 deg. All tests were conducted at the fixed frequency of 1.52 Hz. The reduced frequency k and Reynolds number R, which are defined by using b_f and V_f at 75% semispan station of the forewing are 0.156 and 10.57×10^3, respectively. Perfect hovering at each phase angle Ψ was attained by adjusting the amount and location of the small weights attached at the outside surface of the bottom of the body. As shown in Fig. 16, the real stroke-plane angle ϕ_s can be estimated by measuring the inclination angle ϕ_b of the body centerline by $\phi_s = \phi_s' - \phi_b$, where the geometrical stroke-plane angle ϕ_s is fixed at 20 deg. The time mean lift $\overline{L}_{\text{hover}}$ can also be estimated by measuring the total weight of the robot submerged in the water just after attaining perfect hovering.

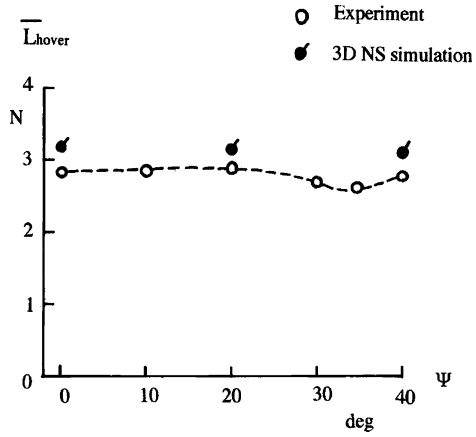

Fig. 17a Comparison of theoretical and experimental total time mean lift.

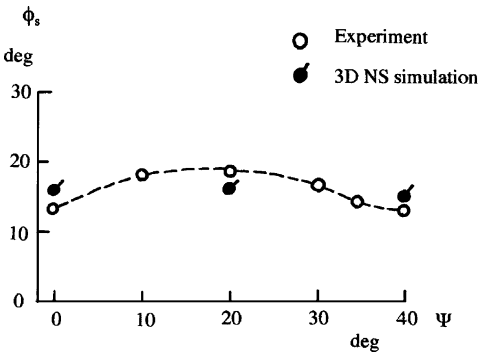

Fig. 17b Comparison of theoretical and experimental stroke-plane angle.

The numerical simulations for these robot wings have been conducted. (The simulations are conducted for exactly the same planform and the motions of the robot wings.) In Figs. 17a and 17b, the theoretical and experimental values of $\overline{L}_{\text{hover}}$ and ϕ_s are plotted with respect to Ψ. As shown in the figures, close agreement between the present NS simulations and experimental data can be obtained, thus validating the present three-dimensional NS code.

V. Conclusions

To clarify the basic aerodynamic mechanism of the hovering flight of the dragonfly, numerical simulations of the unsteady three-dimensional viscous flow around the tandem wing configuration have been performed using a three-dimensional Navier–Stokes code. The flow simulations are conducted for *Anax prthenope julius* as a typical dragonfly model. The total lifting force and specific necessary power predicted by the present simulation show close agreement with those observed experimentally for the present dragonfly model. The present code is further validated by comparing the results of the simulation with experimental values of total lift and stroke-plane angle obtained using a robot.

References

[1]Weis-Fogh, T., "Quick Estimate of Flight Fitness in Hovering Animals, Including Novel Mechanism for Lift Production," *Journal of Experimental Biology*, Vol. 59, 1973, pp. 169–230.

[2]Somps, C., and Luttges, M., "Novel Uses of Unsteady Separated Flows," *Science*, Vol. 228, No. 14, 1985, pp. 1326–1329.

[3]Azuma, A., and Watanabe, T., "Flight Performance of a Dragonfly," *Journal of Experimental Biology*, Vol. 137, 1988, pp. 221–252.

[4]Freymuth, P., "Thrust Generation by an Airfoil in Hover-Modes," *Experiments in Fluids*, Vol. 9, 1990, pp. 17–24.

[5]Wakeling, J. M., and Ellington, C. P., "Dragonfly Flight II. Velocity, Accelerations and Kinematics of Flapping Flight," *Journal of Experimental Biology*, Vol. 200, 1997, pp. 557–582.

[6]Norberg, R. A., "Hovering Flight of the Dragonfly Aeshna Juncea L.," *Swimming and Flying in Nature*, Vol. 2, Plenum, New York, 1975, pp. 763–781.

[7]Savage, S. B., Newman, B. G., and Wong, D. T. B., "The Role of Vortices and Unsteady Effects During the Hovering Flight of Dragonflies," *Journal of Experimental Biology*, Vol. 83, 1979, pp. 59–77.

[8]Gustafson, K., and Leben, R., "Computation of Dragonfly Aerodynamics," *Computer Physics Communications*, Vol. 65, 1991, pp. 121–132.

[9]Wakeling, J. M., and Ellington, C. P., "Dragonfly Flight III. Lift and Power Requirements," *Journal of Experimental Biology*, Vol. 200, 1997, pp. 583–600.

[10]Isogai, K., and Shinmoto, Y., "Numerical Simulation and Visualization of Unsteady Viscous Flow Around an Oscillating Tandem Airfoil in Hovering Mode," *Proceedings of the 2nd Pacific Symposium on Flow Visualization and Image Processing 1999*, edited by S. Mochizuki, 1999.

[11]Wang, Z. J., "Two Dimensional Mechanism for Insect Hovering," *Physical Review Letters*, Vol. 85, No. 10, 2000, pp. 2216–2219.

[12]Isogai, K., and Shinmoto, Y., "Study on Aerodynamic Mechanism of Hovering Insects," AIAA Paper 2001-2470, June 2001.

[13]Lan, S. L., and Sun, M., "Aerodynamic Interactions of Two-Airfoils in Unsteady Motion," *Acta Mechanica*, Vol. 150, 2001, pp. 39–51.

[14]Kim, D., and Choi, H., "Vortical Motion Caused by Two Flapping Wings," *Proceedings of ISABMECH2003* [CD-ROM], Tokai Univ. Pacific Center, Honolulu, HI, 2003, Paper S.3-05.

[15]Isogai, K., Fujishiro, S., Saitoh, T., Yamashaki, M., and Matsubara, M., "Study on Aerodynamic Mechanism of Hovering Flight of Dragonfly by Using a Robot," *Proceedings of ISABMECH2003* [CD-ROM], Tokai Univ. Pacific Center, Honolulu, HI, 2003, Paper S.3-02.

[16]Liu, H., Ellington, C. P., Kawachi, K., Van Den Berg, C., and Willmott, A. P., "A Computational Fluid Dynamic Study of Hawkmoth Hovering," *Journal of Experimental Biology*, Vol. 201, 1998, pp. 461–477.

[17]Thomas, P. D., and Lombard, C. K., "Geometric Conservation Law and Its Application to Flow Computations on Moving Grids," *AIAA Journal*, Vol. 17, No. 10, 1979, pp. 1030–1037.

[18]Yee, H. C., and Harten, A., "Implicit TVD Schemes for Hyperbolic Conservation Laws in Curvilinear Coordinates," *AIAA Journal*, Vol. 25, No. 2, 1987, pp. 266–274.

[19]Pulliam, T. H., and Steger, J. L., "Recent Improvements in Efficiency, Accuracy, and Convergence for Implicit Approximate Factorization Algorithms," AIAA Paper 85-0360, Jan. 1985.

[20]Azuma, A., *The Biokinetics of Flying and Swimming*, Springer-Verlag, Berlin, 1992.

K. Fujii
Associate Editor